Experimental study on fluid energy reduction through a flood protection forest

AUTHOR(S):

Sanjou, M.; Okamoto, T.; Nezu, I.

CITATION:

Sanjou, M. ...[et al]. Experimental study on fluid energy reduction through a flood protection forest. Journal of Flood Risk Management 2018, 11(4): e12339.

ISSUE DATE:

2018-12

URL:

http://hdl.handle.net/2433/252314

EXPERIMENTAL STUDY ON FLUID ENERGY REDUCTION THROUGH A FLOOD PROTECTION FOREST

Michio Sanjou, Takaaki Okamoto and Iehisa Nezu

Department of Civil and Earth Resources Engineering, Kyoto University, Japan, 6158640, Nishikyo-ku, Kyoto. Japan

E-mail: michio.sanjou@water.kuciv.kyoto-u.ac.jp

Abstract

A flood protection forest is a conventional river-management measure that can fit well into the natural environment. This study focused on single-line tree models placed laterally across open-channel flows. We conducted horizontal particle image velocimetry (PIV) and drag force measurements in a laboratory flume to examine the reduction efficiency of mean kinetic energy due to the tree members. The results showed that the flow structure is related closely to a wake phenomenon for sparsely arranged trees, whereas it is similar to a jet for a dense arrangement. It was found that the drag force is related to the separation zone downstream of the trees. In particular, two neighbouring high-speed streaks can merge and become a uniform flow. The characteristic length of this process and incident velocity define the drag force. Furthermore, a semi-theoretical formula was developed that was found reasonable in predicting energy reduction efficiency.

Key Words: *drag force measurement, energy reduction, flood protection forest, jet flow, open-channel flow, PIV measurement and wake phenomenon*

1. Introduction

Robust breakwaters and embankments are required to prevent serious damage by tsunamis, tidal waves and floods. In contrast, a flood protection forest is one of a number

of conventional river-management measures, which has the advantage that its implementation can blend into the natural environment.

In European countries that afforestation is effective in mitigating flood disasters through interception, infiltration, temporary storage, flow deceleration and the prevention of runoff (e.g., Richards et al. 2003; Robinson et al. 2003; Blackwell et al. 2006; Dixon et al. 2016). In Japan, in previous years, bamboo groves and willow trees were planted along the main channels of rivers to prevent bank erosion, attenuate inundation flows and catch driftwood. In particular, the intertwined subterranean root systems reinforced the soils of the floodplain and the riverbank. The use of natural trees for flood protection has many advantages compared with artificial structures because they control water quality via nutrient removal, provide habitats for organisms and have aesthetic benefits for river basin landscapes.

Figure 1 shows an example of an existing flood protection forest. The bamboo grove has been planted along the outer bank of the river in curved sections to slow the flood flow toward the nearby residential area (Fig. 1(a and b)). In particular, the bamboo trees reduce the fluid energy of inundation flows at the dike-break point and reduce runoff toward the houses, although flood damage is not necessarily prevented. Figure 1(c) shows the actual bamboo trees that form the floodplain forest; they are about 15 m high, 10 cm thick and standing at about 50–100 cm intervals.

It is recognized that solid ground, strong foundations and an effective arrangement are very important in the implementation of a natural floodplain forest, such that the trees can withstand the high hydraulic pressure and be effective in reducing fluid energy. However, little is known about the hydrodynamic properties of the flow once it has passed the trees.

The present paper reports the findings of laboratory experiments conducted to measure accurately the formation of the separation layer behind model trees. The relationship between the arrangement interval of the trees and the drag force is considered, and an experimental formula for the energy reduction efficiency of flood protection trees is proposed.

Previous fundamental theories and experimental results considering the drag force acting on a single cylinder help us consider the effects of cylinders in uniform flow, as reviewed by Nepf (1999). The Reynolds number ($\mathrm{Re} \equiv U_m D / \nu$) is a dimensionless quantity used to help predict flow patterns in different flow situations. Here, U_m is a mean reference velocity, D is a cylinder diameter and ν is kinematic viscosity. The wake formed behind an isolated cylinder depends on the Reynolds number, i.e., turbulent structures such as the coherent motions of the shed vortices contribute to the generation of the wake zone that defines the drag force. Williamson (1992) studied the transition from laminar to turbulent flow observed in the wake zone of an isolated cylinder. The principal findings were that a current is stable without large fluctuation when the Reynolds number is low ($\mathrm{Re} < 50$), vortex shedding occurs at Re = 50, and flow instability yields a transition from laminar to turbulent flow when the Reynolds number is large (Re > 200).

Of particular significance here is that the drag force properties of a cylinder array differ markedly from those of an isolated cylinder, as highlighted by Nepf et al. (1997). They reported that in comparison with the case of an isolated cylinder, a cylinder array decreases the drag coefficient, delays the generation of a shear layer and prevents vortex shedding until Re = 150 to 200. Luo et al. (1996) found that the drag coefficient in tandem cylinders depends on the normalized spacing between them. Raupach (1992) proposed two types of wake structure within a cylinder array called sheltering effects. The first is related to the lower incident velocity at the front of a trailing cylinder and the second is related to wake turbulence delaying vortex separation on a trailing cylinder with a decrease of the drag coefficient.

Many experiments have been conducted previously on the wake structure and the drag force of isolated plant and vegetation arrays. The results of such research have contributed to the modelling of the friction force and the local sedimentation induced by river vegetation. Based on the momentum balance, Stone and Shen (2002) considered the total resistance in vegetated flows using channel-bed slope and plant spacing. The total resistance is considered the sum of the plant resistance and the bed shear resistance. The former means the drag force due to plant stems, which can be evaluated by the drag coefficient. Although, the latter (i.e., bed shear stress) governs sediment transport and is

very important for prediction of bottom scouring, it is generally difficult to measure it directly. When the drag coefficient is known precisely, the bed shear stress can be obtained in vegetated flows using the total resistance and the stem drag force. Based on laboratory measurements and dimensional analysis, Kothyari et al. (2009) proposed an experimental formula for the drag coefficient within a cylinder array zone, which is a function of the Froude number ($\mathrm{Fr} \equiv U_m / \sqrt{gH}$, in which g is gravity acceleration and H is water depth), stem Reynolds number and cylinder population.

Nepf et al. (1997) and Nepf (1999) investigated how the developing properties in wake structures contribute to yield the drag force, highlighting the fluid forces on emergent cylinders and the relationship between the wake structures formed behind a vegetation array and the vegetation population. Rominger and Nepf (2011) conducted scale analyses and turbulence measurements in a flow associated with a porous obstruction comprising a cylinder array. They reported that a flow blockage parameter, expressed by the drag coefficient and obstruction scale, controls the behaviour both in the adjustment region upstream of the obstruction and in the interior canopy region.

Tanaka and Yagisawa (2010) conducted hydraulic experiments including drag force measurements for both emergent and submerged vegetation patch conditions. They revealed a relationship between relative depth, stem span, number of model trees forming the vegetation patch and drag force. They observed two types of interesting vortex structure: 1) small-scale Karman vortex street shedding from individual cylinders and 2) a large-scale Karman vortex emerging at the outer edge of the vegetation patch. Nikora et al. (2008) conducted field measurements to evaluate the friction force induced by a submerged vegetation patch within a natural river. Noarayanan et al. (2012) evaluated the energy loss and related roughness coefficient in open-channel flows with emergent cylinder arrays. Interaction between vegetation and currents is important not only in hydraulic engineering but also in meteorology and in wind engineering (e.g., Raupach et al. 1986; Raupach et al. 1996; Finnigan 2000). In particular, friction properties and related scalar transport mechanisms have been studied intensively using data of velocity around trees.

Although much scientific knowledge about the physical effects of vegetation on fluid flows has been acquired, some uncertainties remain regarding the energy reduction

offered by flood protection forests. Water currents lose inherent momentum energy via work against the drag force and the skin friction force due to the trees, which depends on the wake properties formed behind individual trees. For example, a wake structure resembles that observed in uniform flow passing a single cylinder when the distance between two neighbouring trees placed laterally across the flow is large. In contrast, a wake structure resembles a typical jet when the distance between neighbouring trees is small. Furthermore, the arrangement of the trees has considerable effect on the developments of the mixing layer and the separation zone downstream of the trees. Of course, the strength of the incident velocity also plays an important role in wake formation. Because the drag force acting on a specific tree is related to the separation zone behind that tree, in addition to one-dimensional analysis, detailed investigation should also be undertaken of the two- or three-dimensional turbulence structures to reveal the mechanism of drag force generation.

In this study, tree models were placed laterally across a recirculating open-channel flume, and measurements of the horizontal components of velocity and drag force were conducted by varying the arrangement of a population of tree models. We imposed conditions with a low Froude number to avoid inducing free-surface deformation, and we considered the influence of population density on drag force production to propose an experimental formula for the prediction of energy reduction due to the trees.

2. Measurement Procedure

Experimental setup

Figure 2 shows the experiment setup. Laboratory experiments were conducted in a tilting glass flume in which B, D, H and b denote the channel width, diameter of the model trees, water depth and distance between neighbouring trees, respectively. The flume was 10 m long, 40 cm wide and 40 cm high. The water current was generated by a control computer and an electromagnetic flow meter. The bed slope was fixed at 1/1000. We used 26 mm diameter PVC cylinders as the tree models. The PVC cylinders were allocated with constant spacing across the flow 7 m downstream of the channel entrance, where

fully developed turbulent flow was observed under the no-cylinder condition. We chose four patterns of single-line tree density, i.e., tree numbers of n = 1, 3, 5 and 8.

The streamwise, vertical and spanwise coordinates were denoted x, y and z, respectively. Corresponding time-averaged velocity components were defined as U, V and W. The origins $(x, y, z) = (0, 0, 0)$ were selected as the downstream edge of the cylinder, channel bed and centre line of the channel, respectively. The distribution of horizontal velocity components was measured using a standard two-dimensional particle image velocimetry (PIV) system (see Nezu and Sanjou 2011). A 2-mm-thick laser light sheet (LLS) was projected horizontally across the measurement region by a continuous 2-W YAG (non-pulse-like) laser. The projection of a single LLS through one of the glass sidewalls yielded shadow zones behind the cylinders, preventing measurement of the velocities. Hence, two LLSs were projected orthogonally across the measurement zone to prevent the occurrence of shadows, as shown in Fig. 2. The specific density and diameter of the tracer particles were 1.02 and 100 μm, respectively. The spatial and temporal distributions of the tracer patterns were recorded using a high-speed CMOS camera situated over the free surface. The frame rate was 100–500 Hz, depending on the bulk mean velocity. The frame rate corresponded to the time lag between two consecutive images and it was used for calculating the two-dimensional velocity components. A sample rate of 30 Hz, produced by a signal function generator, dictated the time interval between the obtained velocity data. The described horizontal PIV setup covered an image area of 20 × 20 cm with an interrogation window size of 9.9 × 9.9 mm.

In addition to the PIV experiments, the drag force applied to the cylinder located in the centre (middle cylinder) of the array was measured using a digital force gauge (push/pull gauge). The force gauge was fixed horizontally to the cylinder with a 1 mm gap between the cylinder bottom and channel bed. As the middle cylinder was supported only by the force gauge, measured data obtained by the force gauge were concurrent with the drag force acting on the cylinder. The drag force was obtained after time-averaging over 120 s.

Hydraulic conditions

Table 1 shows the hydraulic conditions in the smooth-bed cases. In this study, H was the uniform flow depth far upstream of the cylinders, which was fixed at 15 cm for all cases by adjustment of the tail gate. To prevent influence from secondary currents induced by the sidewalls of the channel, a large aspect ratio condition is required, i.e., a wider width compared with the water depth (Nezu and Nakagawa 1993). However, a smaller depth condition tends to disturb the free surface, which makes it difficult to obtain accurate PIV measurements. Hence, in this study, the water depth was chosen after performing preliminary experiments. In the densest case (n = 8), we compared the drag forces acting on both the middle cylinder and the side cylinder nearest the sidewall for the largest U_m. No significant difference between them was observed and therefore, the sidewall effect was considered too small to influence the drag force.

The reference velocity U_m was the bulk mean velocity 1 m upstream of the cylinder position. The Froude (Fr) and Reynolds (Re) numbers were defined with U_m as Fr $\equiv U_m / \sqrt{gH}$ and $\mathrm{Re} = U_m D / \nu$, respectively. Parameters d and s were the slit width between neighbouring cylinders and the distance between neighbouring slits, respectively, which were used for comparison with previous studies that used two parallel jets. In this study, 10 hydraulic cases were selected by systematically varying U_m and the tree allocation density. The allocation density (b / D) was varied in four patterns for U_m = 15 cm/s, and U_m was varied for the allocation densities of b / D = 1.71 and 3.85.

In the prototype floodplain forest indicated in Fig. 1, the mean stem diameter was about 10 cm, as mentioned above. This implies that the diameter ratio of the prototype to the experimental model was about 1:4. The prototype allocation density b/D = 5 to 10 was comparable with the experimental cases. Furthermore, when flood velocity on the floodplain was assumed 1–3 m/s in the prototype field, the velocity ratio of the prototype velocity to the maximum reference velocity chosen in this experiment was 1:2.5 to 1:7.5. In the prototype, flow depth in previous floods was about 10 m, which corresponds to a value of Fr = 0.1 to 0.3, i.e., comparable with the experimental condition.

The depth variation was very small and thus, accurate PIV measurements could be conducted except for the $n = 8$ ($b / D = 1.71$) condition. Under such flat surface conditions, the refraction effect of the free surface was too small to distort the sampled images. Figures 3 and 4 show the water depth profiles observed in the $n = 8$ cases and related side views of the test region, respectively. It is evident that the variation of depth was more substantial as the bulk mean velocity increased. Locally, the water surface dropped behind the cylinder, contrasting the increase in surface elevation on the upstream side of the cylinder. In particular, higher upstream velocities occurred behind the cylinders. As PIV measurements are very difficult under highly disturbed free-surface conditions, we conducted drag force measurements only for the densest allocation of $n = 8$.

3. Results and Discussion

Horizontal distributions of mean velocity vectors behind model trees

Figure 5 shows the distributions of horizontal velocity vectors and contours of the normalized mainstream velocity U/U_m for cases in which b/D was varied under $U_m = 15$ cm/s. The case where $n = 1$ ($b/D = 7.69$), i.e., a single cylinder placed in the flow, shows a typical symmetrical wake pattern in which boundary layer separation can be observed in the mean flow field. In contrast, the results for $n = 3$ ($b/D = 3.85$) and $n = 5$ ($b/D = 2.56$) are similar to two-dimensional single jets with high-speed streaks. For both allocation patterns, high-speed and low-speed streaks are formed after passing the cylinders. Separation zones accompanied by recirculating flows can be observed behind the cylinders. The drag force yields because of the pressure difference around the cylinder induced by flow separation. When the free-surface variation is very small, an increase of allocation density reduces the cross-sectional area of the passing current, which results in an increase of the velocity in the high-speed streak. Furthermore, the longitudinal length of the recirculating zone corresponding to flow separation becomes larger, and this property has a striking impact on the generation of the drag force, as discussed below.

Comparison of the distributions of normalized mainstream velocity U/U_m for the case

of n = 3 (b/D = 3.85), shown in Fig. 6, suggests that bulk mean velocity has minor influence on the velocity vectors. A relatively fast current can be observed near the cylinder in the high-speed stream zone because the momentum is accumulated there. The velocity difference between the high-speed and low-speed streaks is reasonably large behind the cylinder and lateral mixing has not started. Lateral momentum exchange is promoted by the vortex streets traveling downstream, and a continuous velocity profile is formed in the lateral direction. These velocity distributions and turbulent structures are closely related to the drag force acting on the cylinders; thus, it is important to consider them in detail.

Developing jet structure behind model trees

Complex three-dimensional currents are formed around the cylinder. However, the flow field is expected to be quasi-horizontally two dimensional except for a limited zone very near the cylinder because the horizontal velocity is much greater compared with the vertical velocity. Therefore, the present cylinder-passing flow is comparable with a two-dimensional plane jet phenomenon.

Although the width of a jet increases linearly in the developing region for a single-hole jet phenomenon, neighbouring high-speed streaks meet some distance downstream in the parallel jet-like flows highlighted in this study. This interference of several jet streaks makes the current structure more complex. Figure 7(a) shows the wake flow behind the cylinders classified into four characteristic zones in the streamwise direction. The region in which the existence of the cylinders affects the upstream flow is defined as the upstream zone. The downstream boundary of this zone corresponds to the downstream edge of the cylinders. The upstream boundary corresponds to an imaginary origin, which is discussed later. Immediately downstream of the cylinders, recirculating currents ($U <$ 0) in the area of flow separation and high-speed streaks are formed alternately, and this is called the converging zone. A potential core is formed in the high-speed streak in which the streamwise velocity profile is almost constant in the lateral direction. The high-speed streak supplies momentum to the area of separation, and the recirculating current region changes to a co-current flow with distance downstream. This is defined as the merging

zone, which is where this mixing process of the potential core is promoted significantly.

The width of the high-speed streak can be defined as a half-value of the maximum velocity for the longitudinal position. It increases linearly for a typical single jet. A cross point can be obtained by extending the lines defining the edges of the high-speed streak toward the upstream side. We defined this point as the imaginary origin $(x = x_{io})$ at which the jet, i.e., the high-speed streak, can be assumed to yield. This point is also considered the upstream boundary of the region influenced by the presence of the cylinders. Furthermore, the lateral profiles of velocity and turbulence in this zone are expected to be similar to the typical two-dimensional jet. The longitudinal lengths corresponding to the three zones defined above are given by x_{io}, x_{mp} and x_{cp}, respectively.

With further travel downstream, the low-speed streaks are accelerated and the high-speed streaks are decelerated. This results in the minimum velocity becoming half the maximum velocity and the lateral profile of the streamwise velocity becomes flatter. This zone is defined as the near uniform zone, in which the neighbouring high-speed streaks on the upstream side interact significantly.

The present two-dimensional flow past a single line of trees is compared with the typical situation of two parallel jets, for which many researchers have defined three zones, as shown in Fig. 7(b). In the converging zone just behind the nozzles, the widths of the single-jet structures diffuse in the spanwise direction in the same manner as the corresponding flow past the single-line trees. Of particular significance is that the lateral positions of the peak velocities begin to shift toward each other, which is markedly different from the flow past the single-line trees shown in Fig. 7(a). This results in the intersection of the two jets in the merging zone. Furthermore, the two peak points meet in the combined section and a single jet structure newly appears in the combined zone. The two parallel jets become unified into a single jet structure along an axis aligned between the two nozzles, unlike the flow past the single-line trees. Many previous experimental studies have suggested positions for the locations of the merging section x_{mp} and the combined section x_{cp}. In particular, similarities are expected between the present flow past the single-line trees and the two parallel jets; hence, we compare x_{mp} in detail later in the article.

Figures 8 and 9 show the streamwise variation of the high-speed streak half-width $\delta/2$ obtained from the time-averaged mean flow field. The single-cylinder case of n = 1 is neglected because it is difficult to determine the peak velocity position precisely. The results suggest that the high-speed streak width increases monotonically downstream for all cases because of the momentum exchange with the separation zones.

Although the largest width is observed for the minimum bulk mean velocity under the constant allocation density condition, the rate of increase in the streamwise direction is about 1/10 independent of the bulk mean velocity, as shown in Fig. 8. In contrast, under the same bulk mean velocity conditions, Fig. 9 shows that the rate of increase in the streamwise direction becomes smaller as the number of cylinders increases. The rate of increase of b/D = 2.56 is almost half that of b/D = 3.85 (Fig. 9). The high-speed streak width is larger for sparser allocations, irrespective of the downstream distance from the cylinder. This is because the original high-speed streak width corresponds to the slit width d, which is defined by the cylinder allocation.

The relationship between the imaginary origin x_{io} normalized by D, bulk mean velocity and slit width, i.e., the spacing of neighbouring cylinders, is illustrated in Fig. 10. This figure implies that the imaginary origin is influenced more significantly by slit width than by bulk mean velocity. In particular, the upstream distance from the cylinder is about five times the cylinder diameter D for b/D = 3.85. In contrast, the imaginary origin is positioned further upstream for the smaller slit width, i.e., b/D = 2.56. This corresponds to the smaller variation of high-speed streak width for sparser cylinder allocations, as shown in Fig. 9.

Figures 11 and 12 show the streamwise profiles of U along the x-axis centred on the middle cylinder with varying b/D and U_m, respectively. The spanwise position is indicated by the horizontal dotted line in Fig. 7(a). A zero-crossing point appears in all cases, which represents the downstream boundary of the converging zone. This characteristic zone is related closely to the generation of the drag force, because a larger drag force is expected in the shorter converging zone that corresponds to a smaller normalized spacing b/D. The length of this zone also depends on the bulk mean velocity; specifically, the shortest length is obtained under the minimum velocity condition. Figure 11 suggests that the minimum bulk mean velocity causes the shortest separation lengths behind the cylinders.

The formation of the separation zone is found determined simply by the bulk mean velocity, although there is no clear trend for the U_m > 15 cm/s case. Both x_{mp} and x_{cp} are influenced more by the interval of cylinder arrangement than by the bulk mean velocity, and the development of lateral mixing behind the cylinders occurs more slowly as the distance between neighbouring cylinders is reduced. This results in an increase of the length scales of x_{mp} and x_{cp}. As a detailed discussion of drag force formation is difficult based only on separation length, the measurement of the drag force acting on the cylinders and related energy consumption is discussed later.

Figure 13(a) shows the merging section point x_{mp} measured in the present study together with previous data for the case of two parallel jets. We defined the zero-crossing point between x/D = 1 and 3 in the streamwise velocity profile of Fig. 11. Previous studies on two parallel jets have examined the relationship between the converged section point, normalized by nozzle width x_{mp}/d and normalized nozzle spacing s/d. It is generally known that x_{mp}/d becomes larger with an increase of s/d, as shown in Fig. 13(a). This implies that nozzle spacing is one of the important factors that dominate the hydrodynamic characteristics of the converging zone. Although the normalized spacing s/d is much smaller in the case of the single-line trees compared with the two parallel jets, the common tendency that x_{mp}/d increases with s/d is observed. If the experiments were conducted with a wider channel and larger spacing, i.e., s/d > 5, the normalized converging position x_{mp}/d would be expected to match that of the two parallel jets. Figure 13(b) shows only the present results. Although b/d = 3.85 includes four types of data reflecting the variation of the bulk mean velocity, significant difference is not recognized in the velocity variation compared with the variation of s/d. This suggests that slit width and spacing influence the converging zone corresponding recirculating currents.

Drag force measurements

The definition of the drag coefficient can be described in the following form:

$$C_D \equiv F / \left(\frac{1}{2} \rho A U_m^2 \right), \tag{1}$$

in which the incident velocity is assumed the same as the bulk mean velocity. Figure 14 shows the relation between the bulk mean velocity and the drag force measured by the force gauge. The value of C_D, evaluated using Eq. (1), is expected to have small variation for the velocity range in the present hydraulic condition because the drag force varies as a quadratic function with the bulk mean velocity. In contrast, Fig. 15 shows the variation of the drag force acting on the middle cylinder under a constant bulk mean velocity (U_m = 15 cm/s). It is evident that parallel arrangements increase the drag force compared with the single-cylinder case of b/D = 7.67 (n = 1). This is why the length of the separation region changes with the number of cylinders, as shown in Fig. 13(b).

Figure 16 illustrates the relationship between the drag coefficient C_D and Reynolds number, based on the cylinder diameter D and the bulk mean velocity U_m, in which the results of previous work (JSME 1999) are also included. It is evident that the drag coefficients of the parallel cylinders are 1.1–2.8 times larger than observed for the single cylinder. In particular, the densest cases increase the drag coefficient the most, irrespective of the Reynolds number. The single-cylinder case provides a value of $C_D \cong 1$, corresponding to the previous results; therefore, our force measurements are proven suitably reliable. The variation of C_D is comparatively small for the same arrangement interval over a particular range of Reynolds number (Re = 2000 to 8000).

Energy reduction efficiency

Part of the kinetic energy the water current possesses is lost to the drag force acting on the cylinder. The total energy of the fluid passing the cross section far from the cylinders in unit time E_o can be defined as:

$$E_O \equiv \rho g Q \left(\frac{U_m^2}{2g} + H \right). \tag{2}$$

Considering the ratio of the work per unit time by the water stream to the total friction

induced by cylinders ΔE, the energy reduction efficiency η can be given by:

$$\eta \equiv \Delta E / E_O , \tag{3}$$

in which $\Delta E = nFU_m$.

Figure 17 shows the variation of η with the Froude number for the cases of b/D = 1.71 and 3.85. It can be seen that in the larger velocity case its decrease fits a quadratic-function curve well, irrespective of the number of cylinders. Figure 18 shows the variation of η with normalized slit width b/D for the constant bulk mean velocity of U_m = 15 cm/s. It is evident that the efficiency reduces with increasing slit width, i.e., a denser cylinder arrangement is more efficient in reducing the kinetic energy of the mainstream; specifically, it corresponds to an inverse quadratic-function. Note that neighbouring cylinders touch when b/D = 0.5, and this is the lower limit of the present result.

The results shown in Figs. 17 and 18 allow us to assume that energy reduction is dominated by two non-dimensional numbers, i.e., the Froude number and the allocation density (b/D). Based on a fitting operation using the measured data including hydraulic jump cases, the following experimental formula can be derived:

$$\eta = 1.15 \times Fr^2 (b/D)^{-2}, \quad b/D > 0.5. \tag{4}$$

The R^2 value is 0.98 with only a small scatter in the measured data, as shown in Fig. 19. Although the hydraulic condition is limited to the scale of the laboratory flume, reasonable prediction of the energy reduction in natural flows could be expected when the incident velocity, depth and slit length are known. There is a lower limit, b/D = 0.5, for Eq. (4). Under ultimately dense conditions very close to this limit, trees will choke the flow and the water depth difference between the upstream and the downstream of the trees will become large. Such a flow field has quite different characteristics from the planar two-dimensional flow discussed in this study. In the near future, we are going to perform additional experiments to reveal the critical allocation density corresponding to this flow transition.

For the b/D = 1.71 (n = 8) series, hydraulic jumps are generated behind the cylinders for U_m = 30 and 40 cm/s, as shown in Fig. 4. Hence, in addition to the drag force,

secondary energy reduction due to the hydraulic jump could be expected. The total energy loss between the two sections across the single-line cylinders can be expressed in following form, in which subscripts 1 and 2 refer to the upstream and downstream positions, respectively:

$$\begin{aligned}\Delta E_{total} &\equiv \rho g Q\left(\frac{U_1^2}{2g}+H_1\right)-\rho g Q\left(\frac{U_2^2}{2g}+H_2\right)\\ &=\rho g Q\left\{\left(\frac{U_1^2}{2g}+H_1\right)-\left(\frac{U_1^2H_1^2}{2gH_2^2}+H_2\right)\right\}\\ &=\rho g Q\left\{\frac{U_1^2}{2g}\left(1-\frac{H_1^2}{H_2^2}\right)+H_1-H_2\right\}\\ &\cong \rho g Q\left\{\frac{U_m^2}{2g}\left(1-\frac{H_1^2}{H_2^2}\right)+H_1-H_2\right\}\end{aligned} \quad (5)$$

Figure 20 shows the distributions of total energy loss and the energy loss due to the drag force with Froude number for b/D = 1.71. The test sections 1 and 2 in Eq. (5) are 0.5 m apart from the cylinder position. The loss due to the drag force accounts for most of the total loss for a smaller bulk mean velocity. In contrast, secondary energy loss becomes substantial for bulk mean velocities larger than Fr = 0.247 (U_m = 30 cm/s), and it is three times the energy loss due to the drag force for Fr = 0.371 (U_m = 40 cm/s). This suggests that secondary energy loss attributable to phenomena such as hydraulic jumps is also effective in the overall reduction of energy.

In the experiments of this study, the downstream depth was adjusted by the tailgate, which induced a hydraulic jump. This fact might imply that the secondary energy loss is peculiar to the experimental setup. However, in the prototype field where some banked mounds do exist downstream of the forest, we could expect secondary energy loss in association with the hydraulic jump.

4. Conclusions

This study focused on the energy reduction properties of a flood protection forest, based on horizontal PIV and drag force measurements conducted in a laboratory flume, in which single-line tree models were aligned laterally to the flow. A formula for the prediction of the mean kinetic energy reduction was derived from the experimental results, which can be used with confidence within the range of the hydraulic parameters investigated. The main findings of this study are summarized below.

1) The present horizontal PIV measurements visualized converging zones accompanied by recirculating current flows observed behind the cylinders. The drag force yielded because of the pressure difference around the cylinders induced by flow separation. When the free-surface variation was very small, an increase in allocation density reduced the cross-sectional area of the crossing current, which resulted in an increase in the velocity of the high-speed streaks. Furthermore, the longitudinal length of the recirculating current zone became larger, and this property had considerable impact on drag force generation.

2) It is generally known that the normalized position of the converging section x_{mp}/d becomes larger with an increase of the normalized nozzle spacing in a typical case of two parallel jets. This means nozzle spacing is one of the important factors that dominate the hydrodynamic characteristics of the converging zone. Although the normalized spacing s/d was comparatively small in the present single-line tree flow experiments, s/d increased in the same manner as in the case of two parallel jets. If experiments were conducted with larger spacing, it would be expected that the normalized converging position x_{mp}/d would correspond to that of the two parallel jets. In the present study, significant difference was not recognized in the velocity variation compared with the variation of s/d, and it was found that slit width and spacing had significant roles on the formation of the converging zone and corresponding recirculating currents.

3) The drag coefficients of parallel cylinders were 1.1–2.8 times larger than observed for a single cylinder. In particular, the densest cases increased the drag coefficient the most,

irrespective of the Reynolds number. The single-cylinder case provided a result of C_D = 1, consistent with previous results. The variation of C_D was comparatively small for the same allocation density.

4) Energy reduction efficiency decreased as the slit width increased, implying that a denser arrangement of cylinders would be more efficient in decreasing the kinetic energy of the mainstream. The present results allowed us to assume that energy reduction is dominated by two non-dimensional numbers, i.e., the Froude number and the relative slit length. Based on a fitting operation using the measured data, a linear experimental formula was derived with a high correlation value of 0.99. Note that neighbouring trees touch at b/D = 0.5 and thus, this formula has a lower limit.

5) In the densest (b/D = 1.71, n = 8) series, hydraulic jumps were observed for higher bulk mean velocities. Hydraulic jumps are expected to consume mean kinetic energy. The loss of kinetic energy due to the drag force accounted for most of the total loss for smaller bulk mean velocities. In contrast, secondary energy loss due to the hydraulic jumps became substantial for values larger than Fr = 0.247 (U_m = 30 cm/s). This suggests that secondary energy loss attributable to phenomena such as hydraulic jumps is also effective in the overall reduction of energy.

This study focused on single-line trees as a preliminary stage. It might be difficult to discuss how to plant and manage effective floodplain forests with many rows of trees. Therefore, in the next stage of study, we hope to consider two-dimensional tree allocation, including irregular allocation patterns. For this, a new 2-D density parameter should be suggested instead of b/D for practical use. Further examination under a wider range of Froude and Reynolds numbers and allocation densities is needed to verify the applicability of the presented prediction formula of energy reduction efficiency to the practical design and planning of flood protection forests. All the experiments were conducted under steady flow conditions; however, natural inundation flows and tsunami waves have considerable variation. Therefore, it is very important to understand how flood protection forests might perform under the first effects of such phenomena.

Furthermore, quantitative evaluation of flood damage sustained by buildings downstream of a flood protection forest is another important topic to be considered. We intend to study these subjects using practical experiments and numerical simulations in the near future.

Acknowledgements

The present study was carried out under the financial support from the River Fund of the River Foundation (No. 24-1213-009, Principal Investigator =M. Sanjou) and Grant-in-aid for scientific research (B) (No. 17H03311, Principal Investigator =M. Sanjou). The authors gratefully acknowledge these supports.

References

Anderson, E. A. and Robert, E. S. (2001) Experimental and Numerical Investigation of Two-dimensional Parallel Jets, *J. Fluid Engineering*, 123, 401-406.

Blackwell, M. S. A. Maltby, E., Gerritsen, A. L., Haasnoot, M., Hoffmann, C. C., Kotowski, W., Leenen, E. J. T. M., Okruszko, T., Penning, W. E., Piórkowski, H., Platteeuw, M., Querner, E. P., Siedlecki, T. and de Swart, E. O. A. M. 2006. Ecoflood Guidelines: How to use floodplain for flood risk reduction, European Communities, ISBN 92-79-00962-1.

Dixon, S. J., Sear, D. A., Ondoni, N. A., Sykes, T. and Lane, S. N. 2016. The Effects of River Restoration on Catchment Scale Flood Risk and Flood Hydrology, *Earth Surface Process and Landforms*, 41, 997-1008.

Finnigan, J.(2000) Turbulence in Tree Canopies, *Annual Review of Fluid Mechanics*, 32, 519–572.

Kothyari, U., Hayashi, K. and Hashimoto, H. (2009) Drag Coefficient of Unsubmerged Rigid in Open Channel Flows, *J. Hydraulic Research*, 47 (6), 691-699.

JSME (1999), Mechanical Engineers' Handbook, A5 Fluid Engineering.

Luo, S., Gan, T. and Chew, Y. (1996) Uniform Flow past One (or two in tandem) Finite Length Circular Cylinder(s), *J. Wind Eng. Ind. Aerodyn.*, 59, 69-93.

Militzer, J. (1977) Dual Plane Parallel Turbulent Jets, *Ph.D. Thesis*, University of Waterloo

Miller, D. R. and Commings, E. W. (1960) Force Momentum Fields in a Dual-jet Flow, *Journal of Fluid Mechanics*, 7, 237-256.

Nasr, A. and Lai, J. C. S. (1997) Two Parallel Plane Jets: Mean Flow and Effects of Acoustic Excitation, Experiments in Fluids, 22, 251-260.

Nepf, H. M., Sullivan, J.A. and Zavistoski, R.A. (1997) A Model for Diffusion within an Emergent Tree Canopy, *Limnol. Oceanogr.*, 42 (8), 85-95.

Nepf, H. M. (1999) Drag, Turbulence, and Diffusion in Flow through Emergent Vegetation, *Water Resources Research*, 35 (2), 479–489.

Nezu, I. and Nakagawa, H. (1993) Turbulence in Open-channel Flows, *IAHR Monograph*, Balkema publishers.

Nezu, I. and Sanjou, M. (2011) PIV and PTV Measurements in Hydro-Sciences with Focus on Turbulent Open-Channel Flows, *Journal of hydro-environment research*, 5, 215–230.

Nikora, V., Larned, S., Nikora, N., Debnath, K., Cooper, G. and Reid, M. (2008) Hydraulic Resistance due to Aquatic Vegetation in Small Streams: Field Study, *J. Hydraulic Engineering*, 134(9), 1327-1332.

Noarayanan, L., Murali, K. and Sundar, V. (2012) Manning's 'n' Co-efficient for Flexible Emergent Vegetation in Tandem Configuration, *J. Hydro-environment Research*, 6, 51-62.

Raupach, M. R., Coppin, P. A. and Legg, B. J. (1986) Experiments on Scholar Dispersion within a Model Tree Canopy: Part I The Turbulence Structure, *Boundary-Layer Meteorology*, 35, 21-52.

Raupach, M. (1992) Drag and Drag Partition on Rough Surfaces, *Boundary Layer Meteorol.*, 60, 375-395.

Raupach, M. R., Finnigan, J.J. and Brunet, Y (1996). "Coherent Eddies and Turbulence in Vegetation Canopies: The Mixing-Layer Analogy", *Boundary-Layer Meteorology*, 78, 351–382.

Richards, K., J. Girel, T. Moss, E. Muller, C. Nilsson, and S. Rood. 2003. The Flooded Forest: Guidance for Policy Makers and River Managers in Europe on the Restoration of Floodplain Forests. FLOBAR2. Cambridge: Department of Geography.

Robinson M, Cognard-Plancq AL, Cosandey C, David J, Durand P, Führer HW, Hall R, Hendriques MO, Marc V, McCarthy R, McDonnell M, Martin C, Nisbet TR, O'Dea P, Rodgers M, Zollner A. 2003. Studies of the impact of forests on peak flows and baseflows: a European perspective. *Forest Ecology and Management* 186(1–3): 85–97.

Rominger, J. and Nepf, H. M. (2011) Flow Adjustment and Interior Flow associated with a Rectangular Porous Obstruction, *J. Fluid Mech.*, 680, 636-659.

Stone, B. M. and Shen, H. T. (2002) Hydraulic Resistance of Flow in Channels with Cylindrical Roughness, J. Hydraulic Engineering, 128(5), 500-506.

Tanaka, E. (1970) The Interference of Two-Dimensional Parallel Jets (1st Report, Experiments on Dual Jet). Bull JSME 13, 272-280

Tanaka, N. and Yagisawa, J. (2010) Flow Structure and Sedimentation Characteristics around Clump-type Vegetation, *J. Hydro-environment Research*, 4, 15-25.

Williamson, C. H. K. (1992) The Natural and Forced Formation of Spot-like "Vortex Dislocations" in the Transition of a Wake, *J. Fluid Mech.*, 243, 393-441.

Notation

b lateral distance between centers of neighbouring cylinders

d lateral distance between neighbouring slits

g gravity acceleration

n number of cylinders

s slit / nozzle width

x streamwise coordinate

y vertical coordinate

z spanwise coordinate

B channel width

C_D drag coefficient of middle-part cylinder

D cylinder diameter

E kinetic energy

F drag force acting on middle-part cylinder

$\mathrm{Fr} \equiv U_m / \sqrt{gH}$ Froude number

H water depth

$\mathrm{Re} \equiv U_m D / \nu$ Reynolds number using bulk-mean velocity and stem diameter

U time-averaged velocity in streamwise direction

U_m bulk-mean velocity

W time-averaged velocity in spanwise direction

η energy reduction efficiency

μ viscosity

ν kinematic viscosity

ρ water density

Caption list

Fig.1 Example of flood protect forest in Yura river in Japan: (a) frontal view, (b) backside view, (c)bamboos forming floodplain forest

Fig.2 Experimental setup for PIV measurements and coordinate system: Two laser light sheets are projected to erase shadow behind cylinders. Force gauge is attached to a middle-part cylinder for direct measurement of drag force.

Fig.3 Depth profile in the longitudinal direction for the densest cases (b/D=1.71): Local decrease appears downstream of cylinders in larger attacking velocity

Fig.4 Side views of test region in experimental flume for the densest cases, b/D= 1.71 (n =8)

Fig.5 Comparison of distributions of horizontal mean velocity components (U, W) under constant bulk-mean velocity, U_m =15 cm/s, in which contour means normalized streamwise velocity U/U_m: The velocity difference between the high-speed zone passing cylinders and low-speed one behind cylinders is more remarkable as the allocation density increases. Longer wake structure is observed for the dense case, b/D = 2.56.

Fig.6 Comparison of distributions of horizontal mean velocity components (U, W) under constant allocation density, b/D = 3.85, in which contour means normalized streamwise velocity U/U_m: Though the velocity difference between the high-speed zone passing cylinders and low-speed one behind cylinders is more remarkable as the bulk-mean velocity increases, end point of separation zone corresponding to U = 0 is almost independent of the bulk-mean velocity.

Fig.7 Phenomenological flow models and classification of characteristic zones in the streamwise direction: (a) flow passing one-line cylinders, (b) two parallel jets

Fig.8 Longitudinal variations of high-speed streak half-width varying the bulk-mean velocity under the constant allocation density b/D = 3.85: The minimum bulk-mean velocity induces the largest high-speed streak width. In contrast, spatial increase rate in streamwise direction is independent of the bulk-mean velocity

Fig.9 Longitudinal variations of high-speed streak half-width varying the allocation density velocity under the constant bulk-mean velocity U_m = 15 cm/s: The high-speed streak width is larger in sparser allocation, irrespective of downstream distance from the cylinder, because original width corresponds with the slit width d defined by cylinders allocation.

Fig.10 Relationship between the imaginary origin and the bulk-mean velocity: The imaginary origin is influenced more significantly by the slit width rather than the bulk-mean velocity. In particular, the upstream distance from the cylinder is about five times of the cylinder diameter D for b/D=3.85.

Fig.11 Longitudinal profile of normalized mean streamwise velocity along the axis on the center of middle-part cylinder under the constant bulk-mean velocity: Zero-crossing point appears, which means downstream-side boundary of the converging zone. The converging zone is closely relevant to the generation of the drag force, because larger drag force is generally expected in larger separation zone.

Fig.12 Longitudinal profile of normalized mean streamwise velocity along the axis on the center of middle-part cylinder under the constant allocation density: The smallest bulk-mean velocity case results in the shortest separation length.

Fig.13 Relationship between the merging section point x_{mp} and neighboring slits or /nozzles distance: Though the normalized spacing s/d is much smaller in the present one-line tree flow compared to the two parallel jets, common tendency that x_{mp} increases with s/d is observed.

Fig.14 Relation between the bulk-mean velocity and the drag force on the middle-part cylinder: Drag force varies like a quadratic function with the bulk-mean velocity.

Fig.15 Variation of drag force on middle-part cylinder with the allocation density: parallel arrangements increase the drag force compared to the single cylinder case of n =1.

Fig.16 Relation between Reynolds number and drag coefficient: Drag coefficients of parallel cylinders are 1.1 to 2.8 times as large as that observed in the single cylinder

Fig.17 Relation between bulk-mean velocity and energy reduction efficiency: Larger Froude number case decreases the kinetic energy more efficiently, irrespective of the number of cylinder.

Fig.18 Variation of energy reduction coefficient with allocation density: Denser cylinder allocation decreases the kinetic energy of the coming mainstream more reasonably.

Fig.19 Prediction formula of energy reduction efficiency using two non-dimensional parameters: Proposed linear formula fits reasonably into measured data.

Fig.20 Comparison of energy reduction by cylinders and total energy loss for the most densely allocated cases, b/D = 1.71 (n =8): Energy loss due to the drag force occupies most of the total loss for the smaller Froude number. In contrast, secondary energy loss becomes remarkable for larger velocities and secondary energy loss is also effective to the energy reduction.

Table 1 Hydraulic condition

(a)

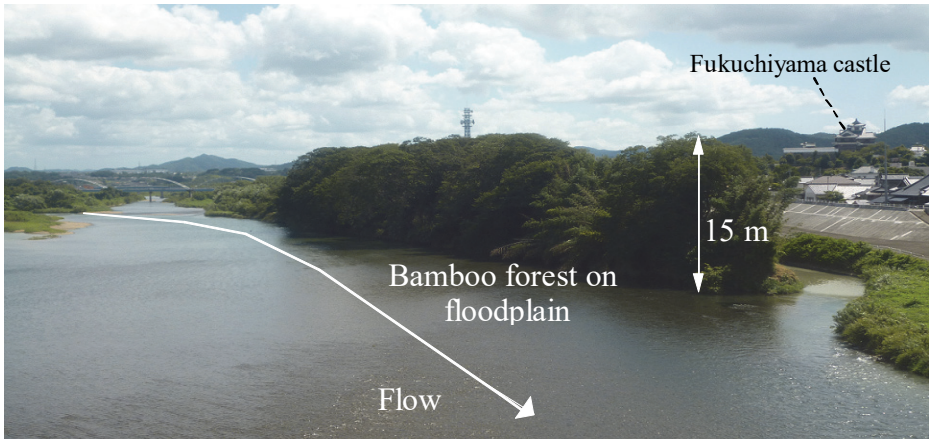

(b)

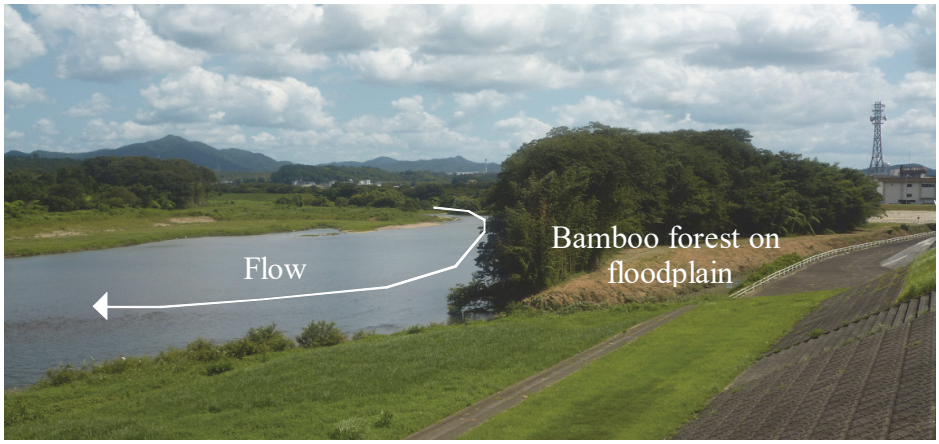

(c)

Fig.1 Example of flood protect forest in Yura river in Japan: (a) frontal view, (b) backside view, (c)bamboos forming floodplain forest

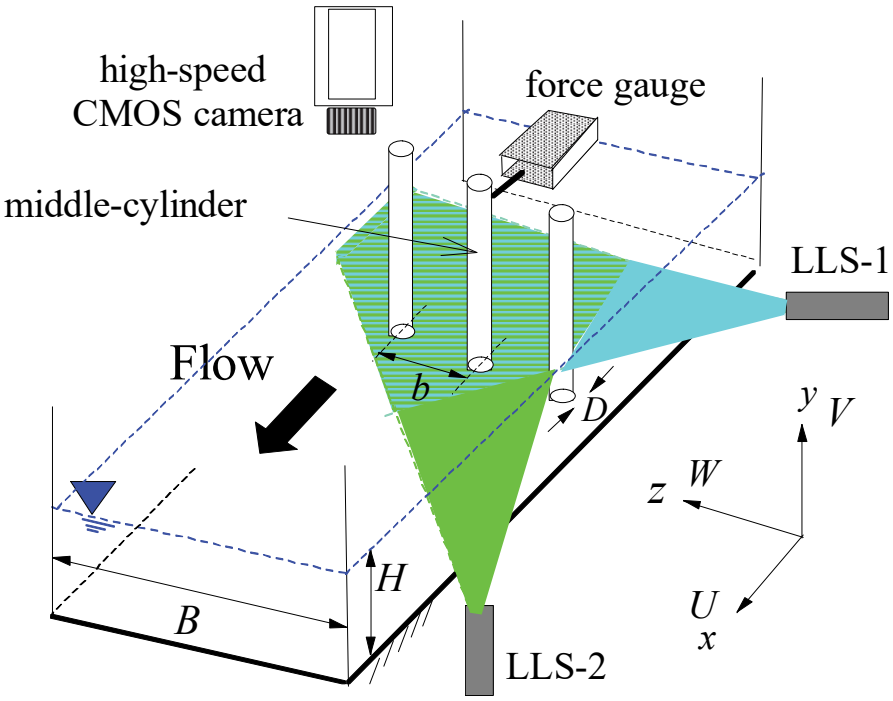

Fig.2 Experimental setup for PIV measurements and coordinate system: Two laser light sheets are projected to erase shadow behind cylinders. Force gauge is attached to a middle-part cylinder for direct measurement of drag force.

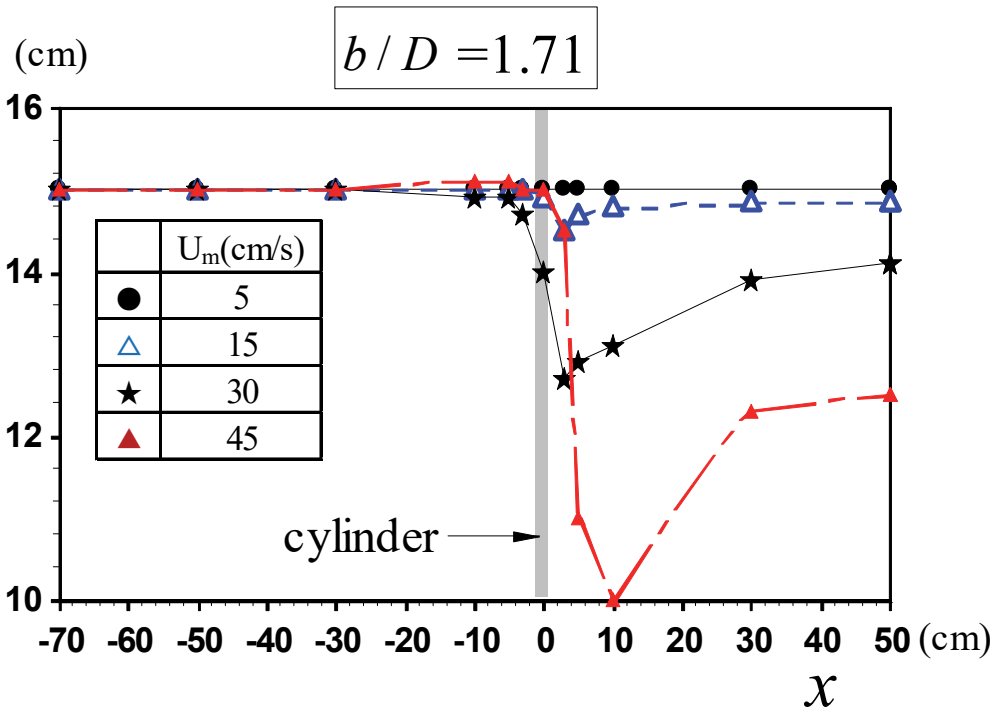

Fig.3 Depth profile in the longitudinal direction for the densest cases (*b/D*=1.71): Local decrease appears downstream of cylinders in larger attacking velocity

(a) $U_m = 5$ cm/s

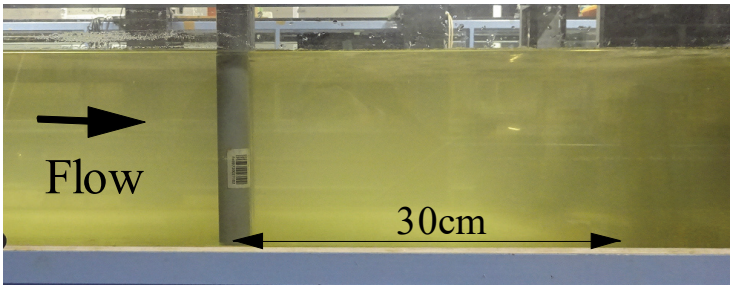

(b) $U_m = 15$ cm/s

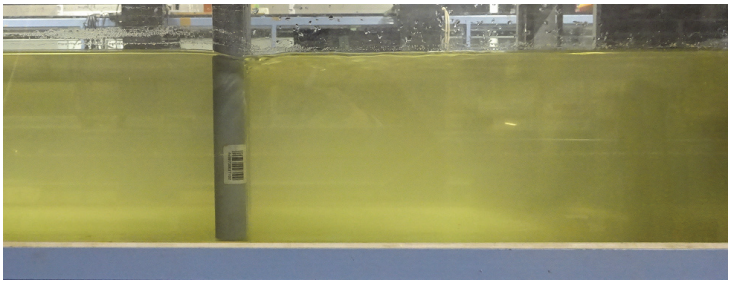

(c) $U_m = 30$ cm/s

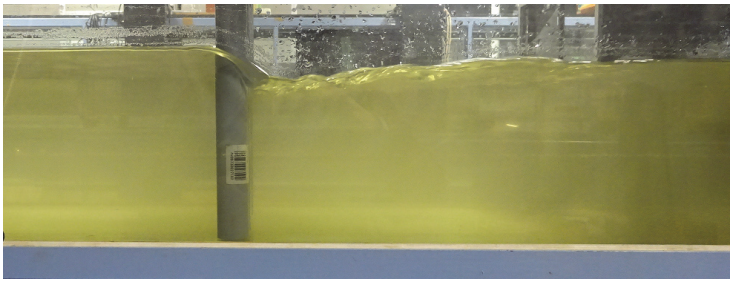

(d) $U_m = 45$ cm/s

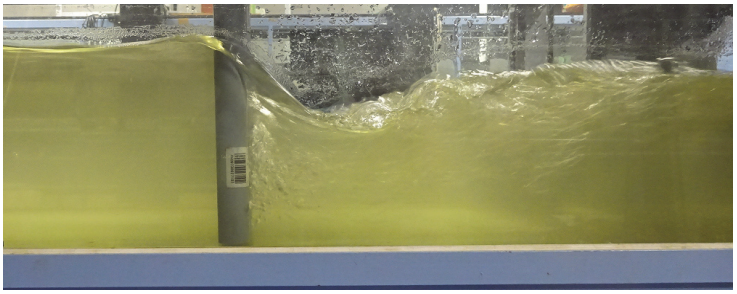

Fig.4 Side views of test region in experimental flume for the densest cases, *b/D*= 1.71 (*n* =8)

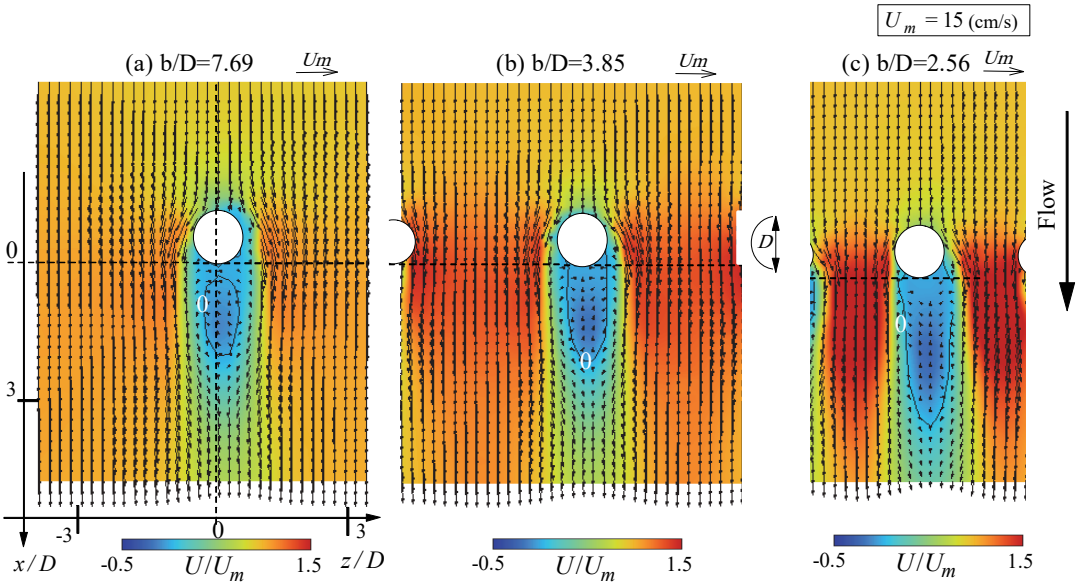

Fig.5 Comparison of distributions of horizontal mean velocity components (U, W) under constant bulk-mean velocity, U_m =15 cm/s, in which contour means normalized streamwise velocity U/U_m: The velocity difference between the high-speed zone passing cylinders and low-speed one behind cylinders is more remarkable as the allocation density increases. Longer wake structure is observed for the dense case, b/D = 2.56.

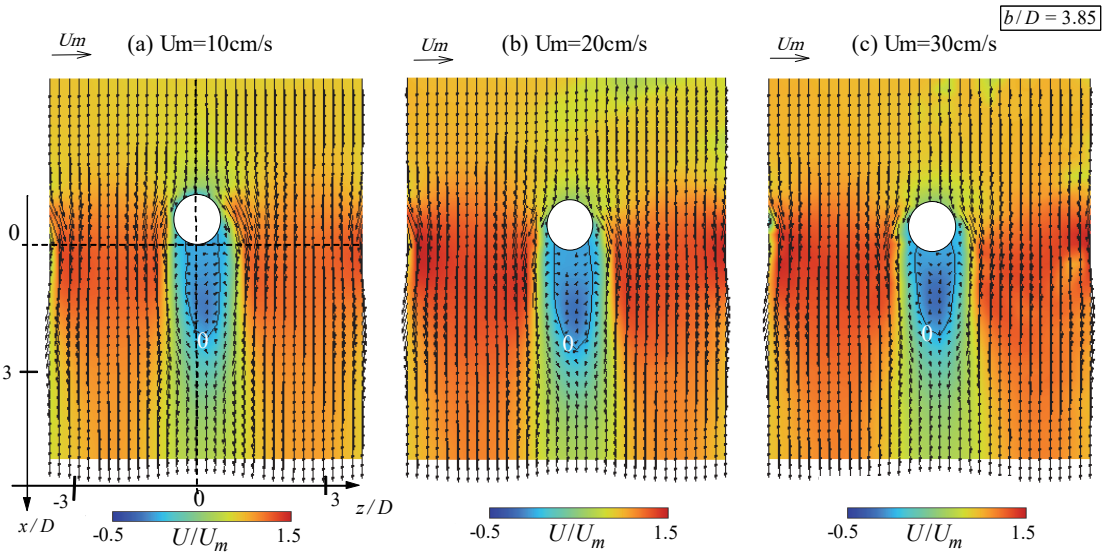

Fig.6 Comparison of distributions of horizontal mean velocity components (U, W) under constant allocation density, b/D = 3.85, in which contour means normalized streamwise velocity U/U_m: Though the velocity difference between the high-speed zone passing cylinders and low-speed one behind cylinders is more remarkable as the bulk-mean velocity increases, end point of separation zone corresponding to U = 0 is almost independent of the bulk-mean velocity.

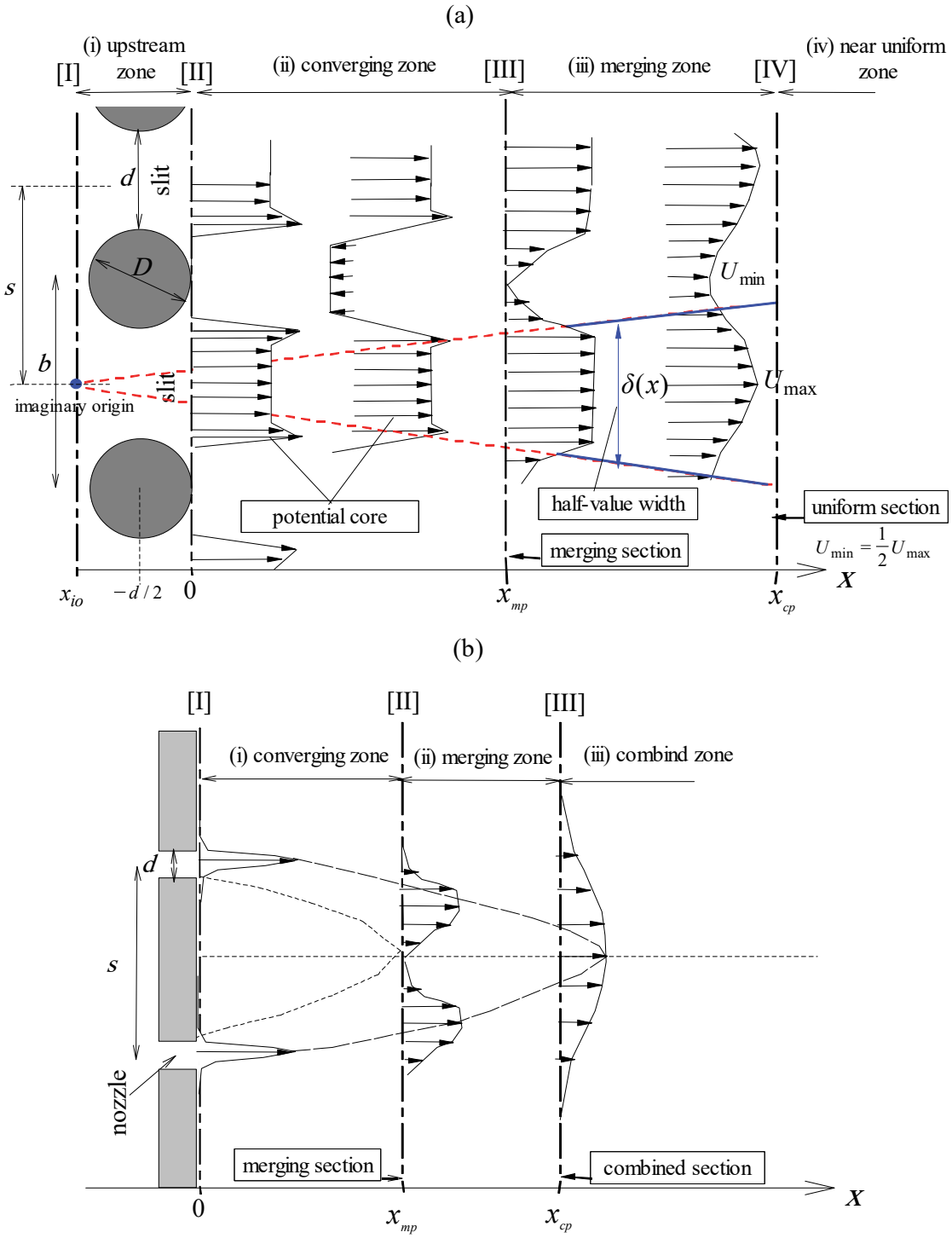

Fig.7 Phenomenological flow models and classification of characteristic zones in the streamwise direction: (a) flow passing one-line cylinders, (b) two parallel jets

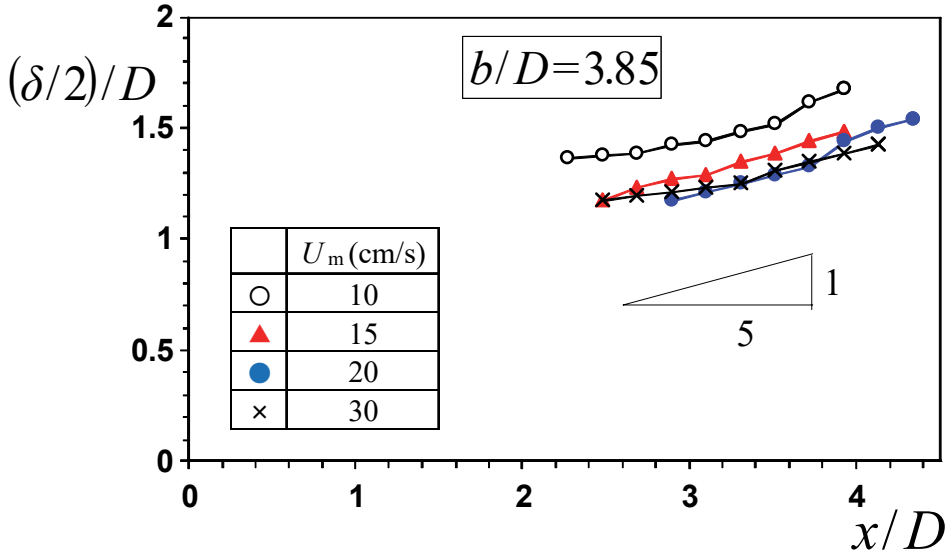

Fig.8 Longitudinal variations of high-speed streak half-width varying the bulk-mean velocity under the constant allocation density $b/D = 3.85$: The minimum bulk-mean velocity induces the largest high-speed streak width. In contrast, spatial increase rate in streamwise direction is independent of the bulk-mean velocity

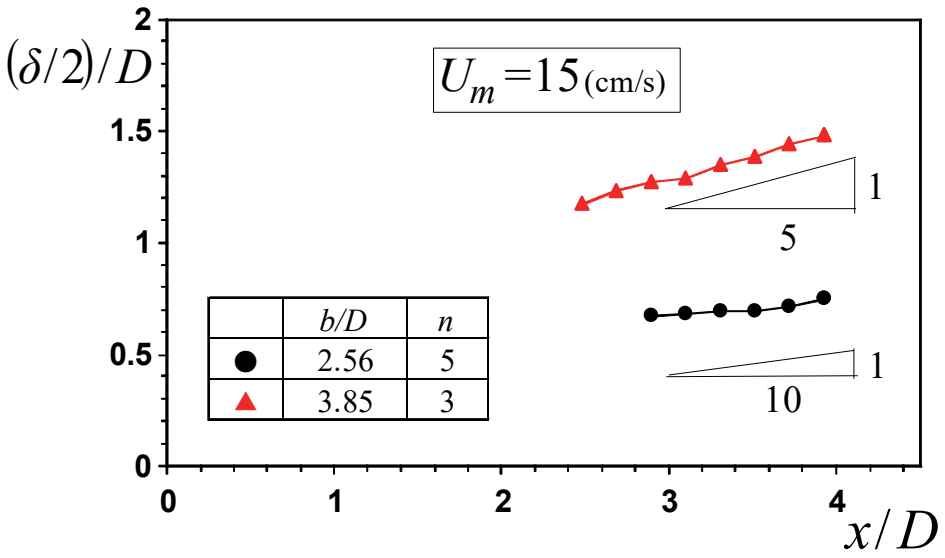

Fig.9 Longitudinal variations of high-speed streak half-width varying the allocation density under the constant bulk-mean velocity U_m = 15 cm/s: The high-speed streak width is larger in sparser allocation, irrespective of downstream distance from the cylinder, because original width corresponds with the slit width d defined by cylinders allocation.

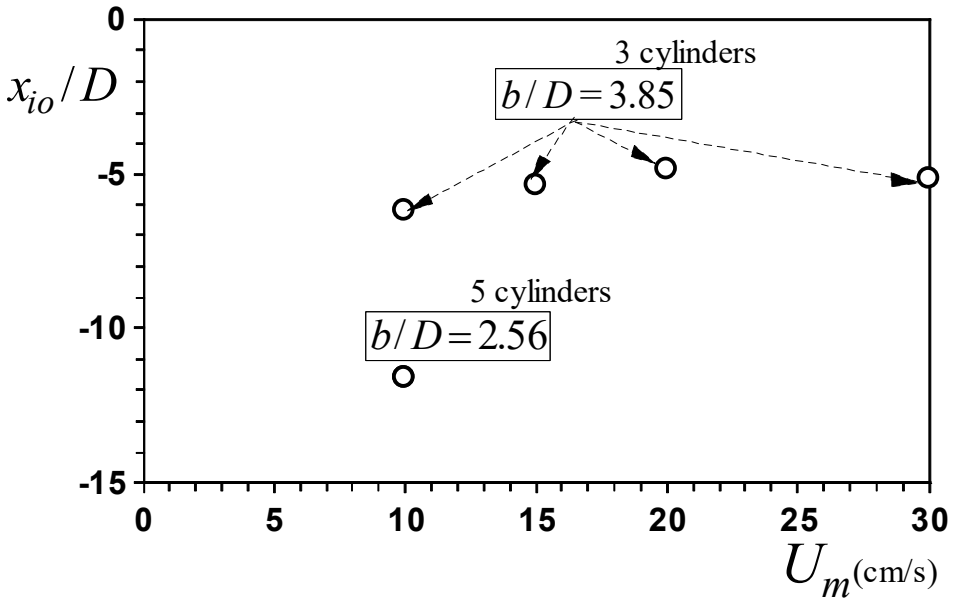

Fig.10 Relationship between the imaginary origin and the bulk-mean velocity: The imaginary origin is influenced more significantly by the slit width rather than the bulk-mean velocity. In particular, the upstream distance from the cylinder is about five times of the cylinder diameter D for b/D=3.85.

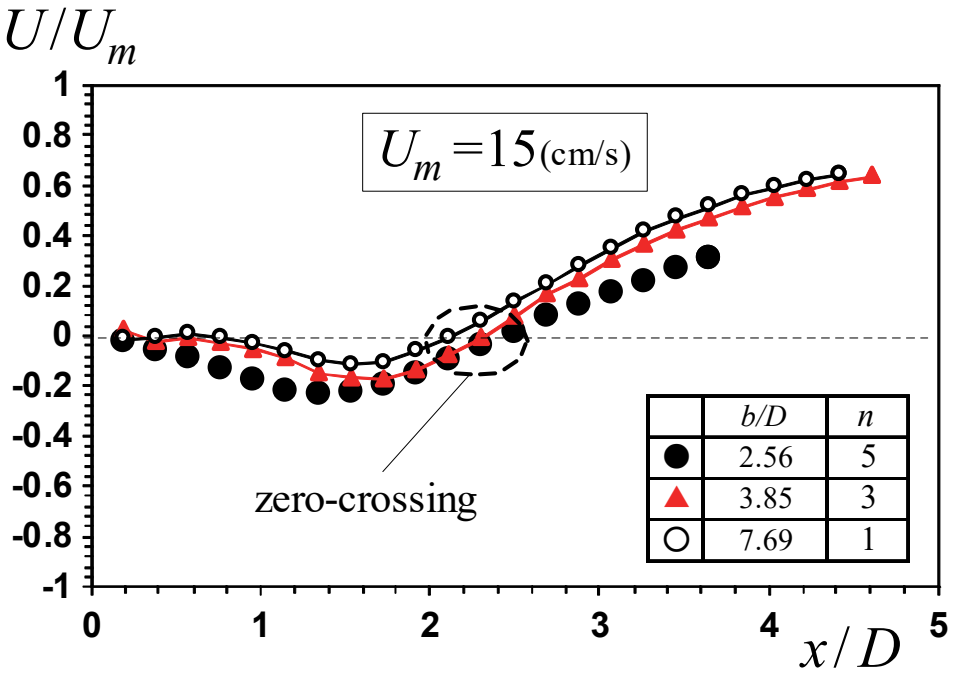

Fig.11 Longitudinal profile of normalized mean streamwise velocity along the axis on the center of middle-part cylinder under the constant bulk-mean velocity: Zero-crossing point appears, which means downstream-side boundary of the converging zone. The converging zone is closely relevant to the generation of the drag force, because larger drag force is generally expected in larger separation zone.

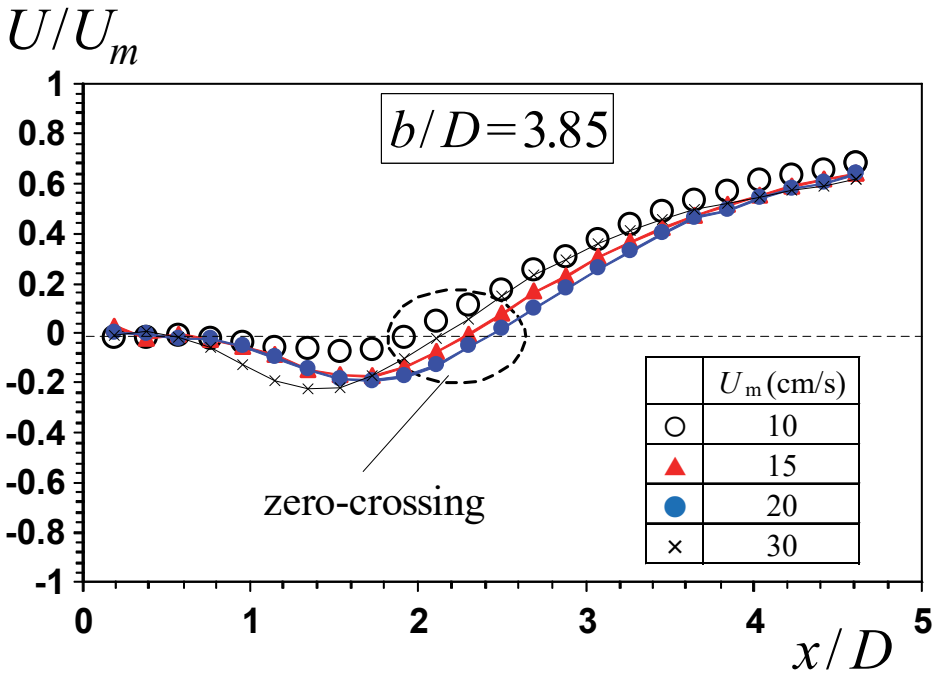

Fig.12 Longitudinal profile of normalized mean streamwise velocity along the axis on the center of middle-part cylinder under the constant allocation density: The smallest bulk-mean velocity case results in the shortest separation length.

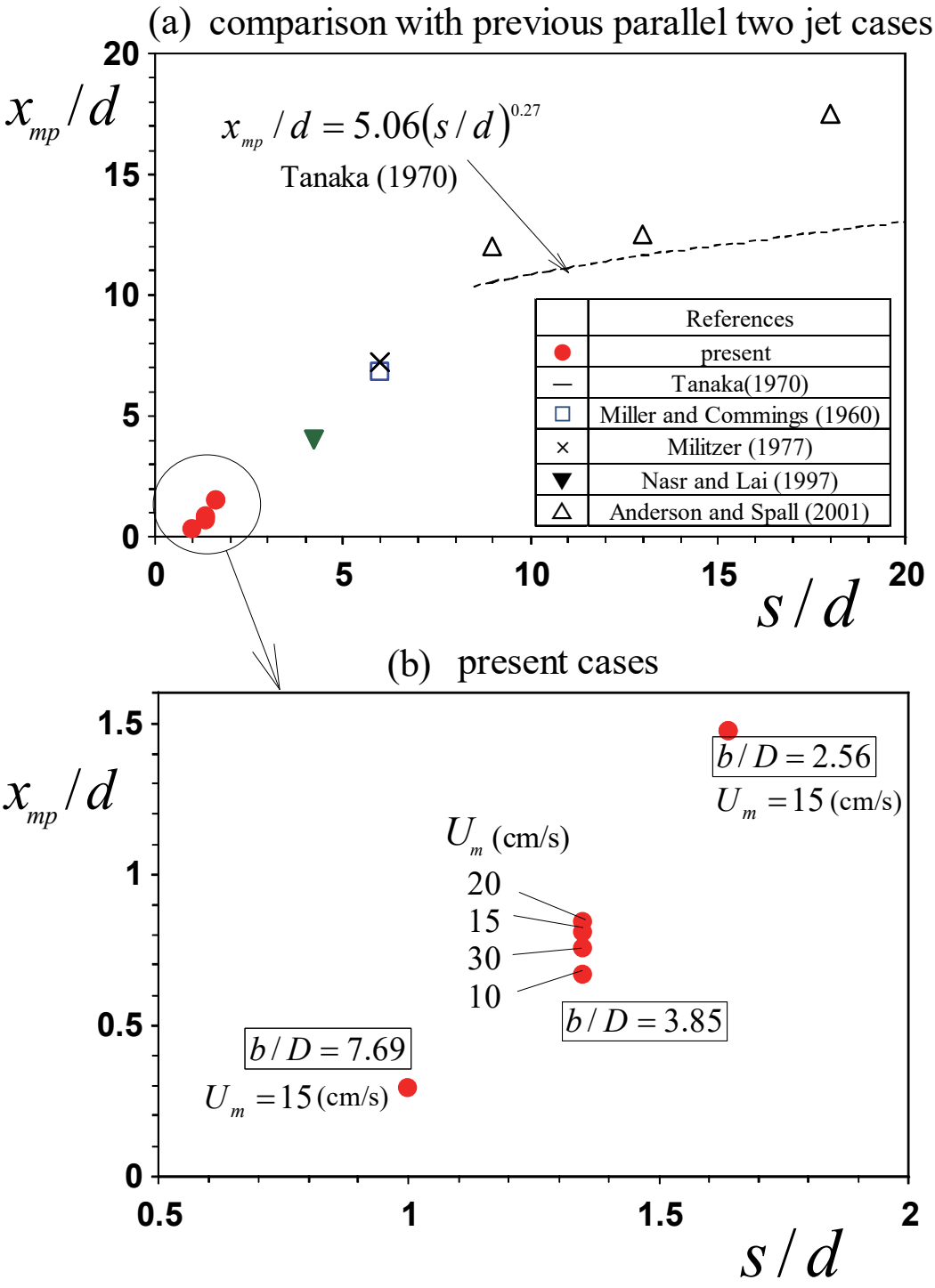

Fig.13 Relationship between the merging section point x_{mp} and neighboring slits or /nozzles distance: Though the normalized spacing s/d is much smaller in the present one-line tree flow compared to the two parallel jets, common tendency that x_{mp} increases with s/d is observed.

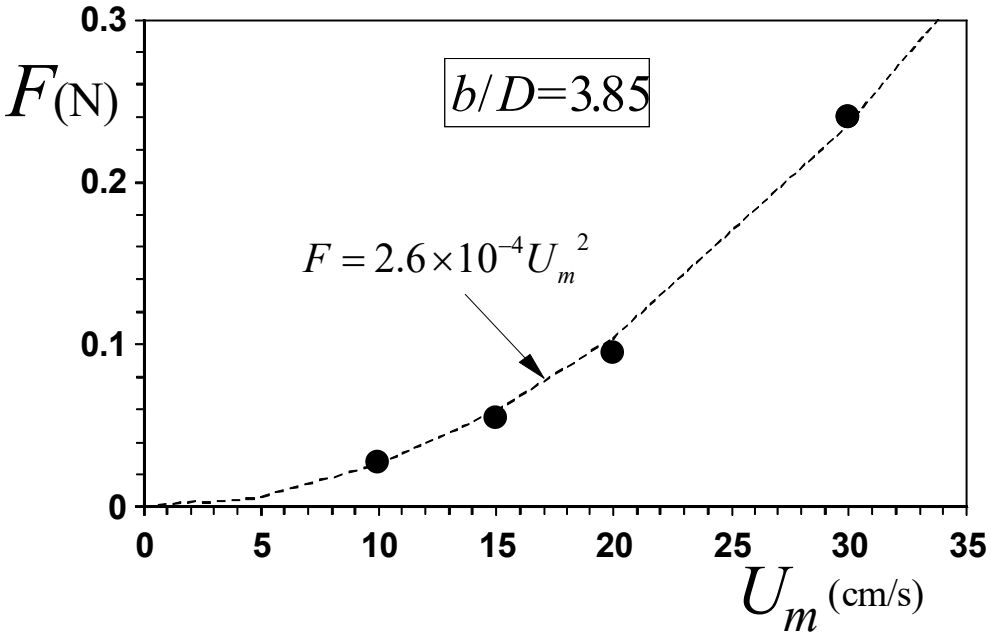

Fig.14 Relation between the bulk-mean velocity and the drag force on the middle-part cylinder: Drag force varies like a quadratic function with the bulk-mean velocity.

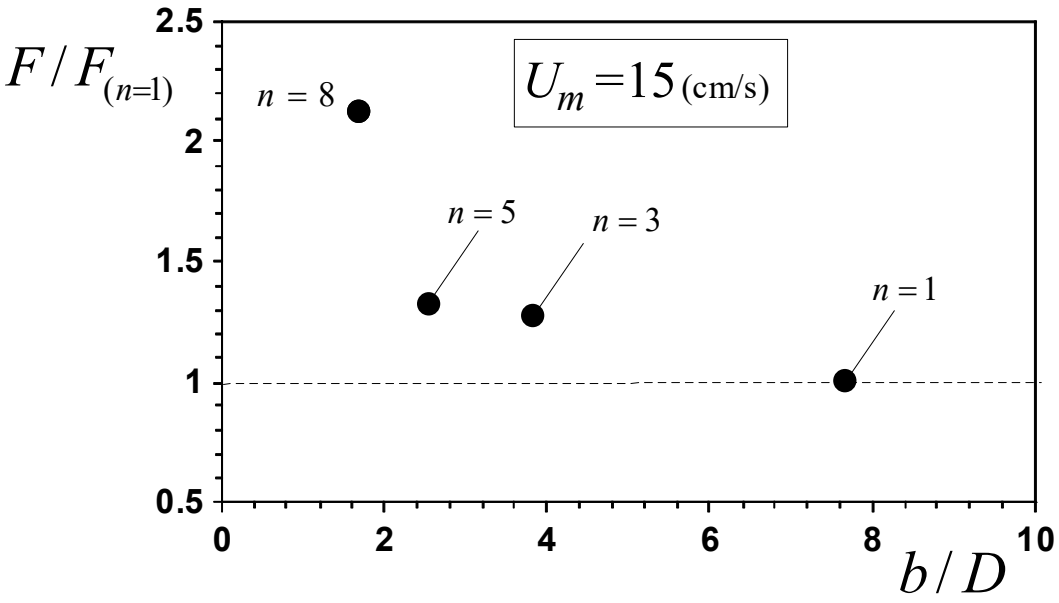

Fig.15 Variation of drag force on middle-part cylinder with the allocation density: parallel arrangements increase the drag force compared to the single cylinder case of n=1.

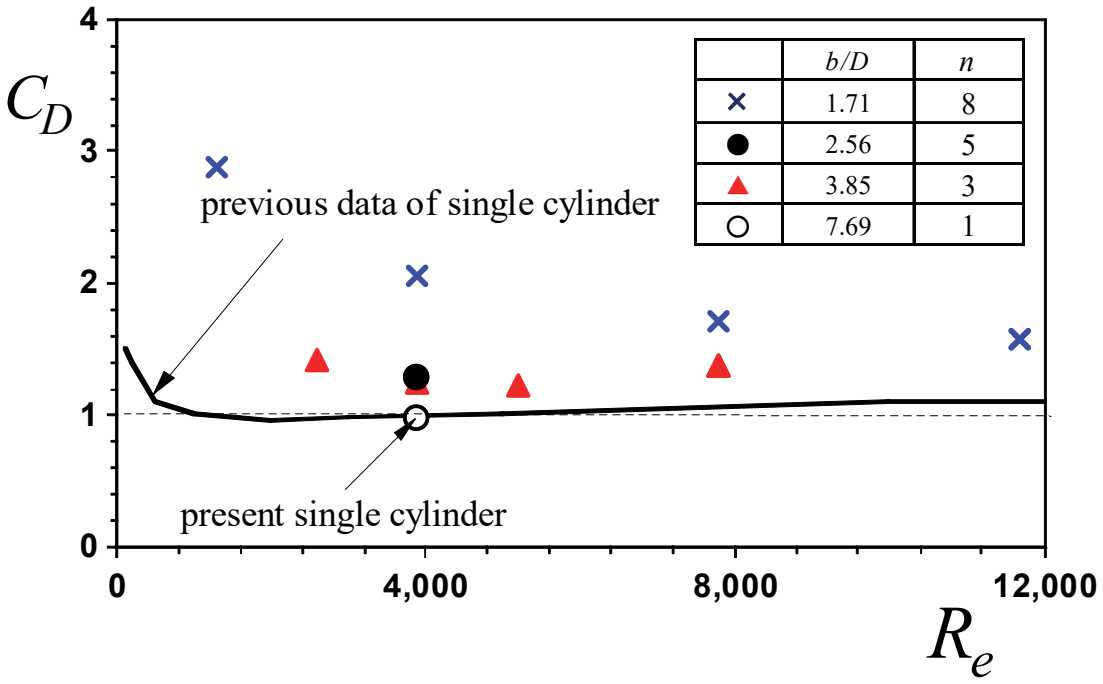

Fig.16 Relation between Reynolds number and drag coefficient: Drag coefficients of parallel cylinders are 1.1 to 2.8 times as large as that observed in the single cylinder

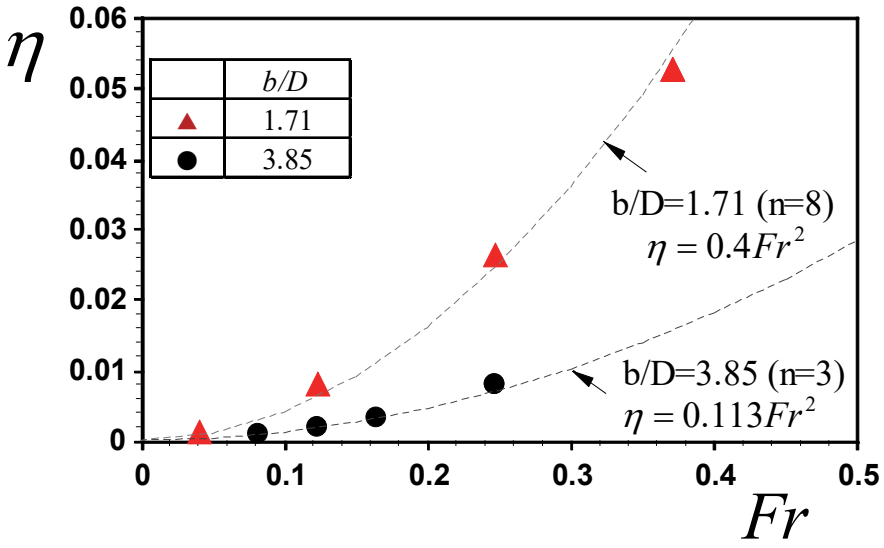

Fig.17 Relation between bulk-mean velocity and energy reduction efficiency: Larger Froude number case decreases the kinetic energy more efficiently, irrespective of the number of cylinder.

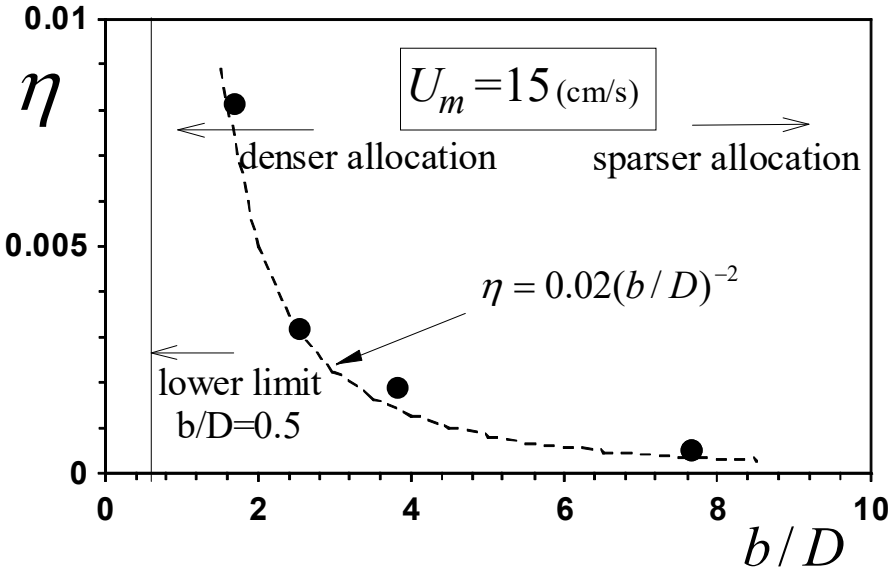

Fig.18 Variation of energy reduction coefficient with allocation density: Denser cylinder allocation decreases the kinetic energy of the coming mainstream more reasonably.

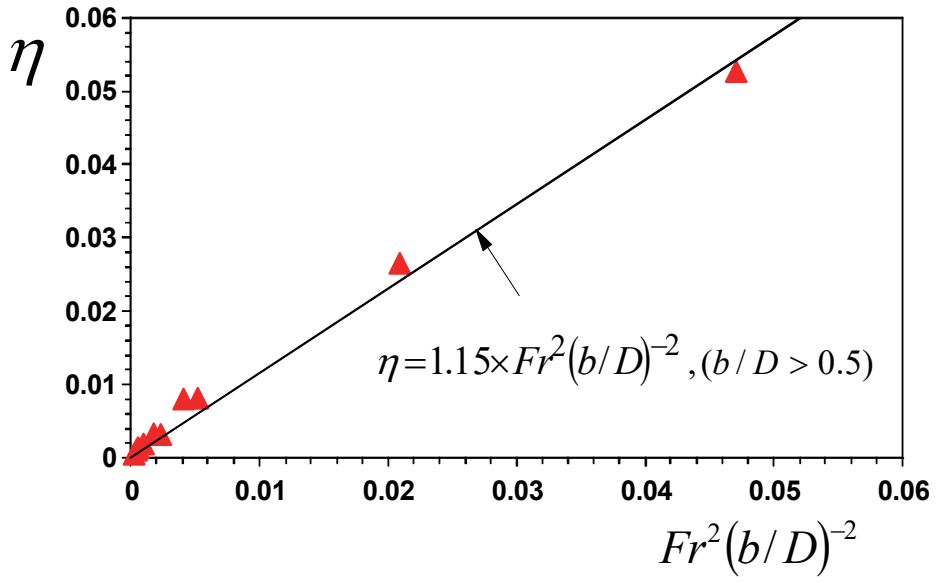

Fig.19 Prediction formula of energy reduction efficiency using two non-dimensional parameters: Proposed linear formula fits reasonably into measured data.

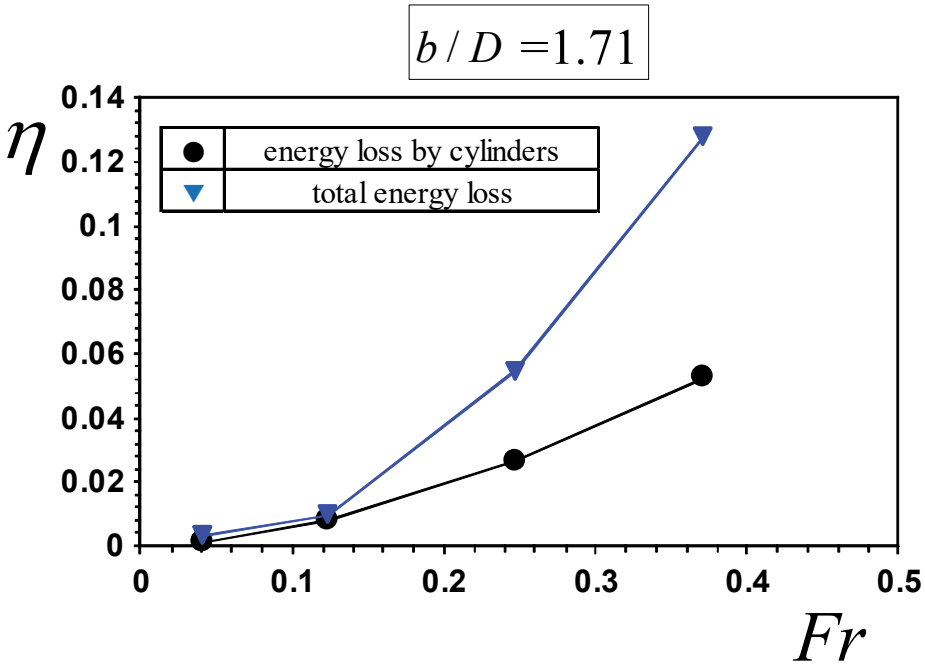

Fig.20 Comparison of energy reduction by cylinders and total energy loss for the most densely allocated cases, b/D = 1.71 (n =8): Energy loss due to the drag force occupies most of the total loss for the smaller Froude number. In contrast, secondary energy loss becomes remarkable for larger velocities and secondary energy loss is also effective to the energy reduction.

Table 1 Hydraulic condition

H (cm)	D (mm)	U_m (cm/s)	Fr	Re	n	b (mm)	b/D	d (mm)	s (mm)	s/d	*experiment*
15	26	15.0	0.124	3900	1	200	7.69	187	187	1	PIV and drag force
		10.0	0.082	2600	3	100	3.85	74	100	1.35	
		15.0	0.124	3900							
		20.0	0.165	5200							
		30.0	0.247	7800							
		15.0	0.124	3900	5	66.5	2.56	41	67	1.64	
		5.0	0.041	1300	8	44.4	1.71	18	44	2.41	drag force
		15.0	0.124	3900							
		30.0	0.247	7800							
		45.0	0.371	11700							